Agricultural and Forest Meteorology 321 (2022) 108975

Contents lists available at ScienceDirect

Agricultural and Forest Meteorology

journal homepage: www.elsevier.com/locate/agrformet

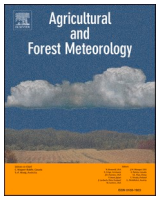

The chained effects of earlier vegetation activities and summer droughts on ecosystem productivity on the Tibetan Plateau

Ning Chen [a], Yangjian Zhang [b,c,*], Changchun Song [a,d,**], Mingjie Xu [e], Tao Zhang [e], Meng Li [g], Nan Cong [b], Jiaxing Zu [f], Zhoutao Zheng [b], Guobao Ma [a], Ke Huang [b,*]

[a] Key Laboratory of Wetland Ecology and Environment, Northeast Institute of Geography and Agroecology, Chinese Academy of Sciences, Changchun 130102, China
[b] Key Laboratory of Ecosystem Network Observation and Modeling, Institute of Geographic Sciences and Natural Resources Research, Chinese Academy of Sciences, Beijing 100101, China
[c] CAS Center for Excellence in Tibetan Plateau Earth Sciences, Beijing 100101, China
[d] School of Hydraulic Engineering, Dalian University of Technology, Dalian 116024, China
[e] College of Agronomy, Shenyang Agricultural University, Shenyang 110866, China
[f] Key Laboratory of Environment Change and Resources Use in Beibu Gulf (Nanning Normal University), Ministry of Education, Nanning 530001, China
[g] School of Geographic Sciences, Nantong University, Nantong 226007, China

ARTICLE INFO

Keywords:
Earlier vegetation activities
Summer drought
Compensate
Carbon uptake
Multiple scales observations
The Tibetan Plateau

ABSTRACT

The knock-on effects between earlier vegetation activities and summer droughts may have important consequences for broad ecological processes. To date, little is known about how the chained effects drive the carbon and water cycles on the Tibetan Plateau (TP). Using the naturally occurring above-mentioned sequential events in spring and summer in 2015 and 2017, we applied the observations at the site, landscape, and regional scales to evaluate the chained effects on the TP. Our findings indicated that higher spring vegetation productivity is caused by early vegetation activities, partially compensated for summer drought-induced loss. Concurrently, increased spring evapotranspiration induced by earlier spring may drain soil water resources earlier, exacerbating summer water restrictions caused mainly by sparse precipitation. This lagged effect of early spring, accompanied by summer drought, significantly increased summer sensible heat flux by 23.2%. Remarkably, the mean air temperature (Ta) was lower than the baseline during drought. This decrease was contributed mainly by lower nighttime Ta, indicating that the region-specific characteristics of the TP could offset the heating effects as mentioned above. The characteristics of high altitude, low air pressure, and thin air could strongly weaken the cloud insulations. More substantial decreases in cloud amount during drought further decreased atmospheric counter radiations, leading to lower mean/nighttime Ta. The simulation results showed that lower mean Ta alleviated the decreases in gross primary productivity by 4.3% through reducing vapor pressure deficit by 5.1%. In conclusion, the present study highlighted the need to comprehensively consider the buffering effects of lower temperature during summer drought to precisely assess the chained effects on the TP.

1. Introduction

The Tibetan Plateau (TP) plays a crucial role in the Asian summer monsoon, with a meteorological system that affects more than half of the world's population (Shen et al., 2015b). The TP ecosystem is highly vulnerable to climate change due to its high altitude and cold climate (Zhang et al., 2019b). In recent decades, the TP has experienced a significant advancing trend of spring greening (Zhang et al., 2013; Zu et al., 2018) and more frequent summer droughts (Bothe et al., 2011; Chen et al., 2013; Li et al., 2018). Earlier vegetation activities have often been reported to increase carbon uptake (Ganjurjav et al., 2021; Zhu et al., 2017). In contrast, summer droughts could exert a significant passive impact on broad ecological processes, and this impact could be stronger than the positive effects of wetting (Chen et al., 2019).

* Corresponding authors at: Key Laboratory of Ecosystem Network Observation and Modeling, Institute of Geographic Sciences and Natural Resources Research, Chinese Academy of Sciences, Beijing 100101, China.
** Corresponding author at: Key Laboratory of Wetland Ecology and Environment, Northeast Institute of Geography and Agroecology, Chinese Academy of Sciences, Changchun 130102, China.
E-mail addresses: zhangyj@igsnrr.ac.cn (Y. Zhang), songcc@iga.ac.cn (C. Song), kehuang@igsnrr.ac.cn (K. Huang).

https://doi.org/10.1016/j.agrformet.2022.108975
Received 16 October 2021; Received in revised form 23 January 2022; Accepted 24 April 2022
Available online 30 April 2022

Recognising that earlier vegetation activities and summer droughts might occur at the same time, a growing number of research have looked into their interconnected consequences on the wide ecological processes (Wang et al., 2020; Wolf et al., 2016). However, the TP is subject to significant uncertainties because the majority of studies have focused on only one aspect of the response of the carbon cycle to the chain effects, such as summer droughts (Xu et al., 2021; Zhang et al., 2019a; Zhang et al., 2018) or spring phenology (Shen et al., 2015a; Shen et al., 2011). As a result, our understanding of the chained effects is quite limited, prompting the need for additional research on the TP.

The compensating effects of earlier vegetation activities on carbon loss caused by summer droughts may come at the cost of earlier soil moisture depletion due to higher spring evapotranspiration (ET), which will likely exacerbate water shortages during the summer drought (Wolf et al., 2016). Extreme droughts have a significant impact on the structure and functions of terrestrial ecosystems, as well as regional carbon balances (Frank et al., 2015). In 2003, the European summer drought reversed four years of net ecosystem carbon sequestration (Janssens et al., 2003). Recently, the United States and European summer droughts have shown that earlier vegetation activities could significantly increase spring carbon uptake, compensating for the summer drought-induced carbon loss (Wang et al., 2020; Wolf et al., 2016). However, this compensation could deplete soil water resources from increased spring ET, thus exacerbating summer water limitations, mainly attributed to scarce precipitation (Wang et al., 2020; Wolf et al., 2016). According to the long time series analysis, there is growing evidence that earlier greening may increase spring ET and so prematurely deplete soil water, leaving the ecosystem more vulnerable to water shortages during the summer (Buermann et al., 2013; Buermann et al., 2018; Lian et al., 2020; Piao et al., 2019; Yu et al., 2018; Zeng et al., 2021).

Significantly, early evaporative water loss caused by earlier greening may result in the emergence of longer-lasting soil water deficits, which could suppresses ET and increases summer sensible heat flux (Lian et al., 2020; Wang et al., 2020; Wolf et al., 2016). This combining with summer drought could further strengthen a positive ecosystem heating feedback (Wang et al., 2020; Wolf et al., 2016). This phenomenon is validated by a wide range of evidence from the arid and semi-arid regions and conforms to the driving processes of higher mean air temperature (Ta) during drought (Fischer et al., 2012; Yin et al., 2014). Despite that, recent research has reported that lower mean Ta is accompanied by summer drought on the TP, especially for nighttime Ta (Chen et al., 2020b). To the best of our understanding, these negative mean/-nighttime Ta anomalies are most likely exclusively documented on the TP. This shows that the TP's region-specific properties could counteract the enhanced heating feedbacks caused by water deficit. High altitude, low air pressure, and thin air on the TP strongly weaken the insulation effects of clouds (Cai et al., 2012). More substantial decreases in cloud amount during droughts further weaken the atmospheric counter radiations and thus could decrease mean/nighttime Ta (Chen et al., 2020b). Moreover, heat propagating downward could be partially consumed by the ice-water phase change in the permafrost regions of the TP (Zhao et al., 2021), which may buffer soil heating during droughts. However, little is known about how lower mean/nighttime temperature influences the response of the broad ecological processes to the linked effects on the TP.

A detailed examination of the chained effects on the TP necessitates a multiscale investigation. The measurements of ground and eddy covariance (vegetation phenology, ET, vegetation productivity, and so on) can help to enhance the mechanistic understanding of the response of ecological processes to climate change (Chen et al., 2020a). However, due to the extreme climate conditions, these observations are sparse and deficient on the TP (Zhang et al., 2019b). It is easy to access and use remote sensing observations across the regional scale, but significant observation errors exist, especially in areas with extreme natural conditions (Parazoo et al., 2018). For instance, in regions with winter snow cover on the TP, remote sensing anticipated green-up dates might be skewed due to preseason snow cover (Huang et al., 2021). Therefore, to overcome the limitations of any single dataset, data synergy is required to analyze the chained effects on the TP.

Naturally occurring earlier vegetation activities and summer droughts during 2015 and 2017 on the TP provided a rare opportunity to investigate the chained effects. We hope to uncover the response of the carbon and water cycles to the linked effects using multiple source datasets that includes direct observations at the site and landscape scales and remote sensing observations at the regional scale. The regional-scale observations of net primary productivity (NPP) and the green-up dates (minimizing the confounding impact of snow cover) have been validated by a large number of ground observation sites (Huang et al., 2021; Li et al., 2021). Based on the multiple source datasets, we aimed to (1) explore the impacts of earlier vegetation activities and summer drought on gross primary productivity (GPP), NPP, and ET; (2) estimate the seasonal compensations and lagged effects of earlier vegetation activities, and (3) examine the underlying mechanisms of these phenomena.

2. Datasets and methods

2.1. Study areas and data scope

The TP (76° 7′–105° 5′ E, 25° 10′–39° 2′ N) is also called "roof of the world," with an average elevation of ~4000 m above sea level and an approximate 2.5×10^6 km^2 of area. The typical vegetation in the alpine grasslands is mainly composed of alpine steppes and meadows (Zu et al., 2018). The site and landscape-scale observations were carried out at alpine meadow in Nagqu (31°38.513′N, 92°0.921′E, 4585 m). Dominant species in this region were *Kobresia pygmaea, Potentilla saundersiana*, and *Potentilla cuneate*.

The targeted growing seasons were set for 2015 and 2017, respectively, for the site, landscape and regional scales observations that satisfied the criterion of early vegetation activities and summer droughts. The baselines were calculated for 2001–2017 (regional scale) and 2012–2018 (site and landscape scale), excluding the drought years. The discrepancies in target growing seasons were primarily due to data collection failures in the spring of 2015, which resulted in poor data quality under landscape-scale observations. Furthermore, we started the site scale observations on June 3, 2017; however, it was postponed until June 19, 2015. Despite this, we fused the observed data from the 2015 and 2017 summer droughts to increase the robustness of the landscape-scale analysis, which included the possible consequences of lower mean Ta. A recent study looked at the anomalies in variables during the 2015 summer drought (Chen et al., 2020b).

2.2. Vegetation phenology observations

Site scale: Using the modified scoring method, the site scale green-up dates of *K. pygmaea, P. saundersiana,* and *P. cuneate* were recorded during the growing season of 2015–2018. Phenology was measured every 3–5 days from May to September. And then, the Richards equation with the contraction-expansion algorithm was applied to fit phenological scores of each species against each day plot (Eq. (1)). These processes were the same as a previous study in our experimental site (Zhu et al., 2017).

$$y(t) = \frac{k}{(1 + a \times e^{-b \times t})^m} \quad (1)$$

Where y represents the phenological stages score, k is the maximum growth, a is the first observation date, b is the growth rate (phenological stage change per day) over time t (days since the first observation date), and m is a curved shape-related parameter.

Landscape-scale: GPP is extensively used to estimate vegetation phenology using phenological extraction functions (Huang et al., 2021; Wang et al., 2019). In this study, a logistic model was applied to extract the green-up dates during 2012–2018 (Eq. (2)) (Zhang et al., 2003).

$$y(t) = \frac{c}{1 + e^{a+b\times t}} + d \quad (2)$$

Where t is time in days, $y(t)$ is GPP at time t, a and b are the fitting parameters, $c+d$ is the maximum GPP, and d is the initial background GPP (Zhang et al., 2003).

The rate of change in the curvature (RCC) of the fitted logistic models is used to identify phenological transition dates (Eq. (3)).

$$RCC = b^3 cz\left\{\frac{3z(1-z)(1+z)^3\left[2(1+z)^3 + b^2c^2z\right]}{\left[(1+z)^4 + (bcz)^2\right]^{\frac{5}{2}}} - \frac{(1+z)^2(1+2z-5z^2)}{\left[(1+z)^4 + (bcz)^2\right]^{\frac{3}{2}}}\right\} \quad (3)$$

Where $z = exp^{(a\ +\ bt)}$. When vegetation transitions from a dormant state to maximum leaf area during the growth period, the first local maximum value of RCC is defined as the green-up date (Zhang et al., 2003).

We used the Quasi-Newton and Universal Global Optimization in 1stOpt 1.5 (First Optimization; 7D-Soft High Technology Inc. Beijing, China) to estimate the parameters of phenology models in the site and landscape-scale observations.

Regional-scale: We used plant phenology index (PPI) and normalized difference phenology index (NDPI) to estimate the green-up dates during 2001–2017. Based on the 21 ground-based sites, our recent studies showed that PPI and NDPI performed well for both snow-free and snow-covered sites on the TP (Huang et al., 2021). The Asymmetric Gaussian was utilized to reconstruct the PPI and NDPI time series in TIMESAT, and then extracted the green-up dates (Huang et al., 2021; Zu et al., 2018).

2.3. LAI, NPP, and GPP observations

Site scale: GPP was measured by an infrared gas analyzer (IRGA; LI-6400, LiCor Inc.) attached to a transparent chamber (0.3 × 0.3 × 0.3 m^3). Two small electric fans were installed inside the chamber and ran continuously to mix the air inside to ensure air uniformity in the static chamber. GPP was measured every 5–7 days from 9:00 a.m.–12:00 a.m. from May to September in 2015–2018.

Landscape-scale: The open-path eddy covariance system, including an infrared gas analyzer (Model LI-7500A, Li-cor Inc., Lincoln, NE, USA), was used to measure GPP at 2.3 m above the ground during 2012–2018. The flux data were collected at 10 Hz, then resampled to 30 min average by a CR3000 datalogger (Model CR3000, Campbell Scientific).

We collected landscape-scale observations of leaf area index (LAI) in the MOD15A2H (4-day, 500 m) (https://modis.ornl.gov/globalsubset/). Each LAI image was sampled by picking pixels covering the flux tower over the desired time interval. The LAI data utilized in this study were acquired like that applied in previous landscape-scale investigations (Li et al., 2016).

Regional-scale: The Carnegie-Ames-Stanford approach model was used to estimate monthly NPP with a spatial resolution of 1 km (CASA; Eq. (4)). CASA is a light consumption efficiency model, with its NPP defined primarily by absorbed photosynthetically active radiation (APAR) and light energy conversion (ε) (Potter et al., 1993) as follows:

$$NPP = APAR \times \varepsilon = fPAR \times PAR \times \varepsilon^* \times T_\varepsilon \times W_\varepsilon \quad (4)$$

$fPAR$ is the fraction of the incoming photosynthetically active radiation intercepted by green vegetation, which NDVI can calculate; ε^*: the maximum possible light energy conversion efficiency; T_ε and W_ε: unitless scalars for temperature and water stress coefficients. This CASA NPP dataset used in our study was validated by 362 ground sites on the TP (Li et al., 2021). The simulated NPP corresponded well with the field-measured ones, with an R-squared more than 80% (Li et al., 2021).

The global, OCO-2-based SIF product (GOSIF) and linear relationships between SIF (Solar-induced chlorophyll fluorescence) and GPP were used to map GPP globally from 2001 to 2017 at 0.05° spatial resolution and monthly timestep (http://globalecology.unh.edu/data/GOSIF-GPP.html) (Li and Xiao, 2019). The datasets mentioned above were accumulated into 0.05° × 0.05° spatial resolution and one-month temporal resolution.

2.4. ET, drought indexes, and meteorological observations

Landscape-scale: ET was measured using an open path infrared gas (H_2O) analyzer (LI-7500; LI-COR). The soil water content (SWC), soil temperature (TS), Ta (nighttime, daytime, and mean), relative humidity (RH), net radiation (RN), downward shortwave radiation (DR), downward long radiation (DLR; nighttime, daytime and mean), latent energy (LE), sensible heat flux (H), and precipitation were simultaneously measured by a meteorological station near the flux tower. The SPI_SL_6 was utilized to calculate the one-month standardized precipitation index (SPI).

Vapor pressure deficit (VPD) in the landscape scale was calculated from mean Ta and RH in Eq. (5) (Zhang et al., 2018).

$$VPD = 6.11 \times \exp\frac{17.27 \times Ta}{Ta + 237.3} \times \left(1 - \frac{RH}{100}\right) \quad (5)$$

Regional-scale: GLASS ET (0.05° × 0.05°; 8 days) was estimated by five traditional LE algorithms using the Bayesian Model Averaging, including MODIS, the revised remote sensing-based Penman-Monteith, the Priestly-Taylor Jet Propulsion Laboratory, the modified satellite-based Priestley-Taylor and the semi-empirical Penma algorithm (Yao et al., 2015a; Yao et al., 2015b). The validation results show that GLASS ET reduces the uncertainty of a single algorithm and ensures the precision and quality of products (Yao et al., 2015a).

Monthly DR and precipitation during 2001–2017 were directly derived from the China Meteorological Forcing Dataset (CMFD) at a 0.1° spatial resolution (He et al., 2020b). By averaging the three-hourly products for the corresponding period in CMFD, monthly daytime Ta, nighttime Ta, and nighttime DLR were synthesized. GLEAM v3.5a monthly root-zone SWC was calculated using a multi-layer running-water balance with a spatial resolution of 0.25° from 2001 to 2017 (Martens et al., 2017). The Standardized Precipitation Evapotranspiration IndexIndex (SPEI) used in this study was derived from SPEIbase v2.5 at a 0.5° resolution and one-month timescale (http://spei.csic.es/database.html).

The mean Ta, air pressure (p), and specific humidity (q) in CMFD from 2001 to 2017 with a spatial resolution of 0.1° was obtained He et al., 2020a). Then we used month p, mean Ta, and q to calculate monthly VPD in the regional scale observations according to Eqs. (6), ((7), and (10) (Ding et al., 2018).

$$VPD = e_s - e_a \quad (6)$$

The saturated vapor pressure (e_s) was calculated using Eq. (7).

$$e_s = 6.11 \times \exp\left(\frac{17.27 \times Ta}{273.3 + Ta}\right) \quad (7)$$

The actual water vapor pressure (e_a) is related to the mixing ratio (r), as shown in Eq. (8).

$$r = \frac{0.622 \times e_a}{p - e_a} \quad (8)$$

The mixing ratio is very close to the specific humidity (Wallace and Hobbs, 2006), as shown in Eq. (9), since r << 1.

$$q = \frac{r}{1 + r} \approx r \quad (9)$$

The e_a was then calculated according to Eq. (10).

$$e_a = \frac{p \times q}{0.622 + q} \quad (10)$$

The datasets, as mentioned above, were uniformly gathered into the spatial resolution of 0.1° × 0.1° and temporal resolution of one month.

2.5. Statistical analyses

The statistical differences in the anomalies of variables were analyzed using a one-way ANOVA and a one-sample *t*-test. The pathways that could explain the drivers of the anomalies in GPP and ET at the landscape scale were investigated using structural equation modeling (SEM). In spatial grid-scale, the partial correlation analysis (PCOR) was used to investigate the driving factors of the anomalies in the green-up dates, vegetation productivity, and ET. PCOR was also applied to analyze the lagged impact of spring ET on summer SWC, and the Granger causality test was used to quantify causality. To estimate the driving factors of nighttime Ta anomalies and quantify the relative contributions of the independent variables at the landscape and regional

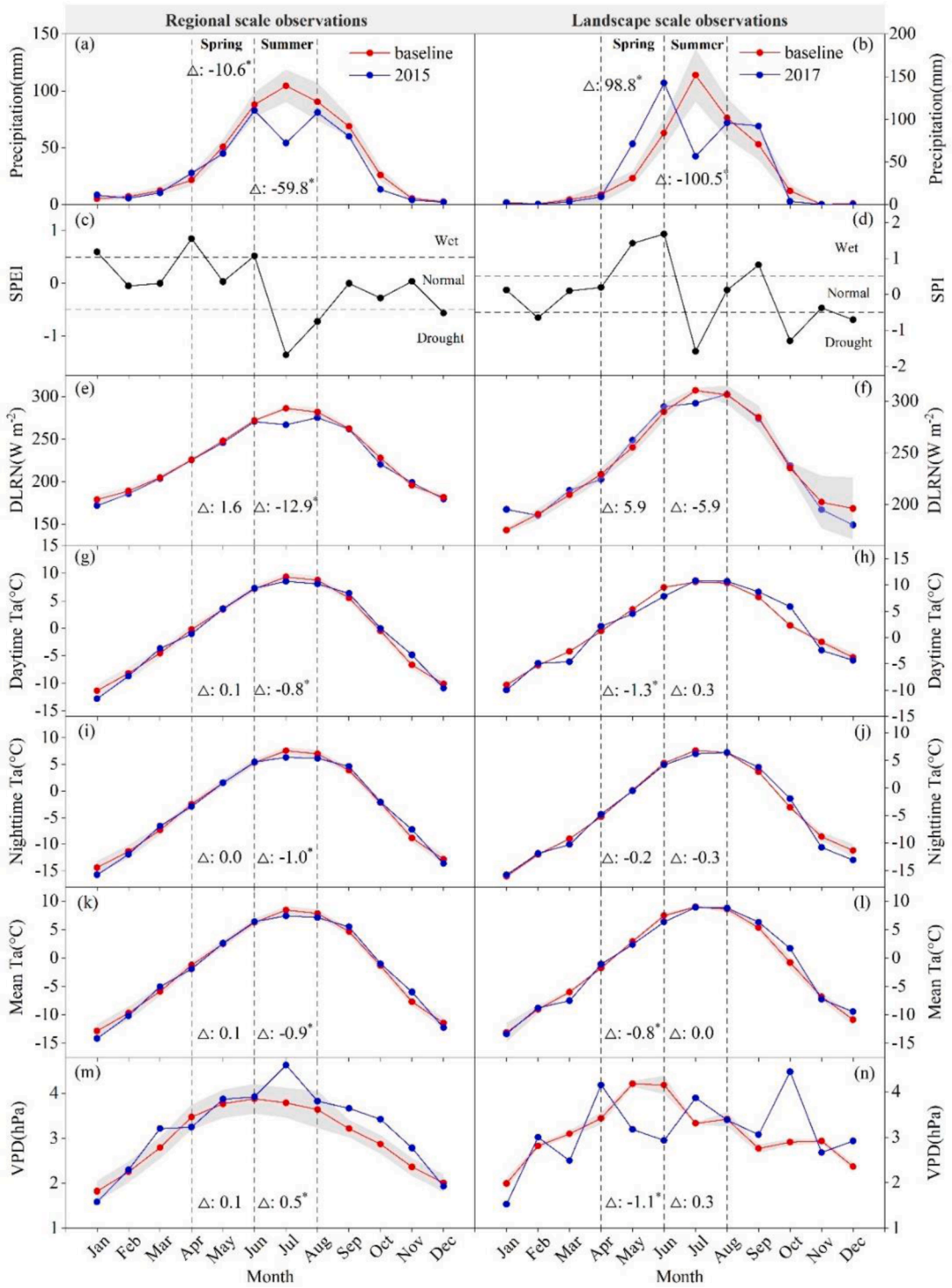

Fig. 1. The monthly dynamic of the environmental variables for the target growing seasons and baseline under regional and landscape scales observations. (a, b). Precipitation, (c, d). Drought indexes, (e, f). Nighttime DLR (DLRN), (g, h). Daytime Ta, (i, j). Nighttime Ta, (k, l). Mean Ta, and (m, n). VPD. "Δ" indicated the target growing seasons minus the baseline, and "*" represented the differences were significant ($p < 0.05$). Spring: May and June; Summer: July and August.

scales, multiple linear regressions (MLR) and random forest models (RF) were employed. RF was also applied to simulate the potential effects of lower mean Ta on GPP during summer drought in this study. First, we established the training models using observed values during the summer drought and then exported predicted GPP ($GPP_{Control}$). Second, baseline mean Ta replaced observed mean Ta, and VPD was replaced by the simulated values calculated by baseline mean Ta. Third, we applied the same training models to export predicted GPP ($GPP_{Simulated}$) based on this scenario simulation. The differences between $GPP_{Control}$ and $GPP_{Simulated}$ were defined as the potential effects of lower mean Ta on GPP through changing VPD. These analyses were conducted in R 4.0.3 (http://www.r-project.org/) software (The instructions of parameter optimization in the RF are available in Appendix S1).

3. Results

3.1. The environmental variable anomalies under multiple scales observations

The average spring precipitation deficits were 10.6 mm on a regional scale, while precipitation was generally higher than the baseline in the mid-eastern TP (Figs. 1a and A.1). Spring precipitation was significantly higher ($p < 0.05$) than the baseline of 98.9 mm at the landscape scale (Fig. 1b). Precipitation deficits during summer (particularly in July) were significant in the landscape and regional scales, with the magnitude of 100.5 mm (July; 94.9 mm) and 59.8 mm (July; 50.3 mm) less than the baseline ($p < 0.05$), respectively (Fig. 1a,b). Summer precipitation deficits occurred in most of the study area (Fig. A.1). The SPEI and SPI for both scales were consistent with the precipitation variability (Figs. 1c,d and A.1).

The anomalies of spring nighttime DLR differed insignificantly relative to the baseline for both scales (Fig. 1e,f; $p > 0.05$). The significant decreases ($p < 0.05$) in nighttime DLR were 12.9 W m^{-2} and 12.4 MJ m^{-2} (July) during summer at the regional and landscape scales, respectively (Figs. 1e,f, A.1 and A.2). Nearly 90% of the study area exhibited negative anomalies of nighttime DLR during summer (Fig. A.1). Summer daytime Ta and nighttime Ta were 0.8 and 1.0 °C significantly lower ($p < 0.05$) than the baseline under the regional scale, respectively (Fig. 1g,i). These negative anomalies of Ta occupied more than 75% of the study region, which were also spotted in the meteorological stations (Figs. A.3 and A.4). Though summer mean Ta was close to the baseline, July nighttime Ta was significant 0.6 °C cooler, resulting in mean Ta of 0.2 °C lower than the baseline (Figs. 1h,j,l and A.2). In summer, VPD was significantly increased ($p < 0.05$) by 0.5 hPa (July: 0.8 hPa) at the regional scale (Fig. 1m). Similarly, the landscape observation of VPD was significantly 0.5 hPa higher ($p < 0.05$) than the baseline in July (Fig. 1n).

3.2. The anomalies of the green-up dates and vegetation productivity under multiple scales observations

Under the site-scale, the green-up dates of *K. pygmaea, P. saundersiana*, and *P. cuneate* were significantly advanced ($p < 0.05$) by 12, 11, and 8 days, respectively, compared to the baseline (Fig. 2a). Similarly, compared to the baseline, the green-up date was 9 days earlier under the landscape scale (Fig. 2b; $p < 0.05$). According to regional-scale observations, more than 70% of the study region experienced earlier vegetation activities. Compared to the baseline, the green-up dates were on average 3 days earlier (Fig. 2c,d; $p < 0.05$).

Spring GPP was 55.6 g C m^{-2} and 19.0 g C m^{-2} greater than the baseline ($p < 0.05$) under the site and landscape scales, respectively (Fig. 3a). Similarly, spring NPP and GPP increased significantly ($p < 0.05$) by 5.6 g C m^{-2} and 5.4 g C m^{-2} under the regional scale, respectively (Fig. 3a,b,d). The positive anomalies mainly appeared in

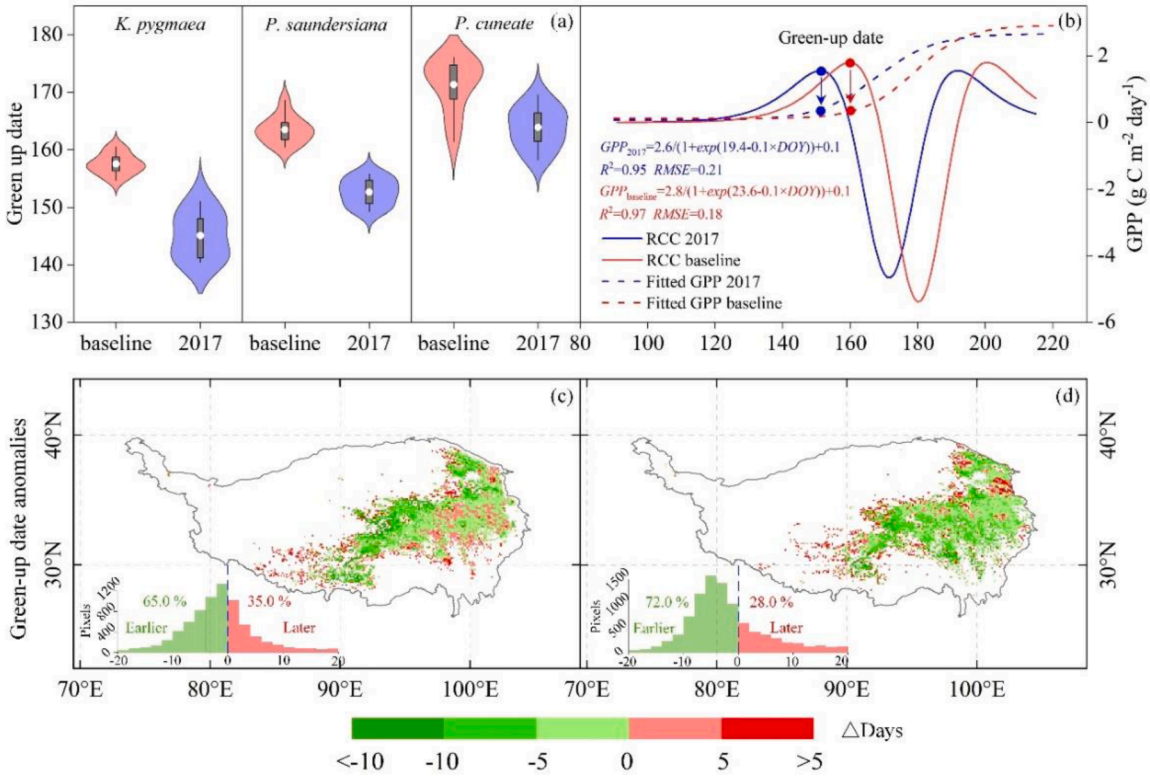

Fig. 2. The anomalies of the green-up dates under the multiple scales observations. (a). Site scale; (b). Landscape-scale; (c, d). Regional-scale of NDPI (c). and PPI (d). (a). White dots in the violin plots indicated the mean of the green-up dates. (c, d). The pixel values indicated the anomalies of the green-up dates, and the density distributions of the anomalies are shown in the bottom-left corner of each panel. (For interpretation of the references to color in this figure, the reader is referred to the web version of this article.).

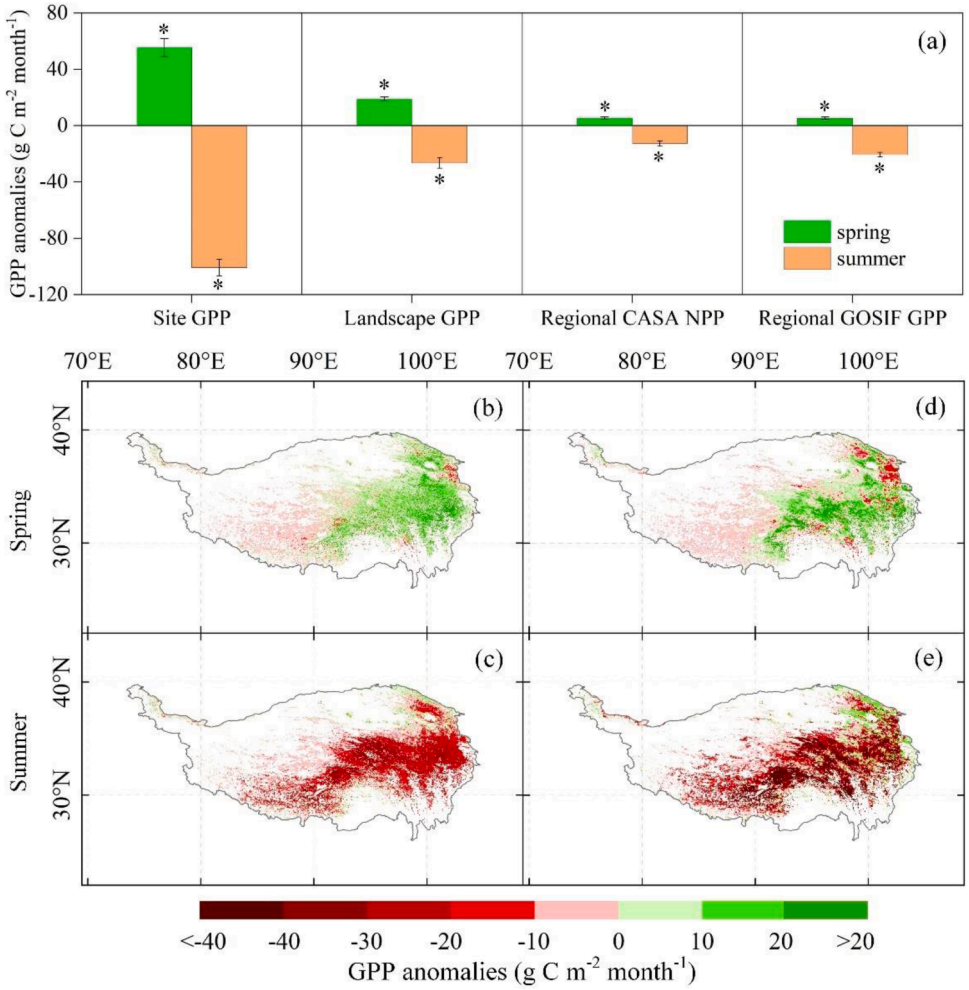

Fig. 3. The anomalies of vegetation productivity under multiple scales observations. (a). The anomalies of GPP and NPP at three scales; (b-e). The spatial distribution of the anomalies in NPP (b, c) and GPP (d, e) during spring and summer. "*" indicated significant ($p < 0.05$) anomalies.

the mid-eastern TP (Fig. 3b,d). In contrast, summer GPP decreased significantly ($p < 0.05$) by 100.7 g C m^{-2} and 27.7 g C m^{-2} under the site and landscape scales (Fig. 3a). Likewise, during summer, the NPP and GPP were 12.75 g C m^{-2} and 20.49 g C m^{-2} lower significantly than the baseline ($p < 0.05$) under the regional scale, respectively (Fig. 3a,c,e). Three-scale observations consistently demonstrated that increased spring vegetation productivity could partially compensate for the summer declines.

3.3. *The anomalies of the water and heat fluxes under multiple scales observations*

At the landscape scale, spring LE (62.0 MJ m^{-2}), ET (25.4 kg H_2O m^{-2}), and total soil water storage (TWS) (42.1 mm) were significantly higher ($p < 0.05$) than the baseline during spring (Fig. 4a–c). Compared to the baseline, evaporative cooling through LE (ET) was significantly reduced by 29.0 MJ m^{-2} (−11.9 kg H_2O m^{-2}), with some of the excess energy released through increased H (+14.0 MJ m^{-2}) during summer (Fig. 4a,b; $p < 0.05$). Summer TWS (51.0 mm) was significantly lower than the baseline ($p < 0.05$) under the landscape scale (Fig. 4c). Regional-scale observations of the variability in ET and SWC showed similar anomalies (Fig. A.5). ET and SWC during spring were significant 2.5 W m^{-2} and 0.01 m^3 m^{-3} higher than the baseline ($p < 0.05$), respectively, and more than 65% of the study region experienced these increases (Fig. A.5). In summer, the negative anomalies of ET and SWC occupied approximately 70% of the study area, and ET and SWC were significantly lower than the baseline by 4.9 W m^{-2} and 0.01 m^3 m^{-3}, respectively (Fig. A.5; $p < 0.05$).

We then examined the lagged effects of increased spring ET on subsequent SWC at the landscape and regional scales. On the one hand, precipitation deficits were 76.3 mm during the early summer drought, while ET was 11.0% higher than the baseline (Fig. 4b,e). Increased ET, partly due to more vigorous vegetation activity (GPP anomalies > 0 increase), may increase TWS consumption, thereby exacerbating the water deficit during subsequent drought (Fig. 4d). On the other hand, at the landscape scale, we observed the significant negative correlations between spring ET and summer TWS (Table 1; $p < 0.05$). Similarly, more than 50% of the study area (about 25% with a significant negative correlation) experienced above negative correlations under the regional scale (Fig. 5a; $p < 0.1$). The negative regions mentioned previously densely distributed across the mid-eastern TP, with the majority of them overlapping with the area of higher spring ET than the baseline (Fig. 5a). Furthermore, at the landscape and regional scales, the Granger causality test revealed that spring ET was the Granger cause of summer SWC/TWS (about 94% of the significant negative correlations accorded with Granger reason) (Table 1; Fig. 5b). These results suggested that increasing spring ET could deplete soil water resources earlier, thus exacerbating summer water limitations mainly driven by decreasing precipitation.

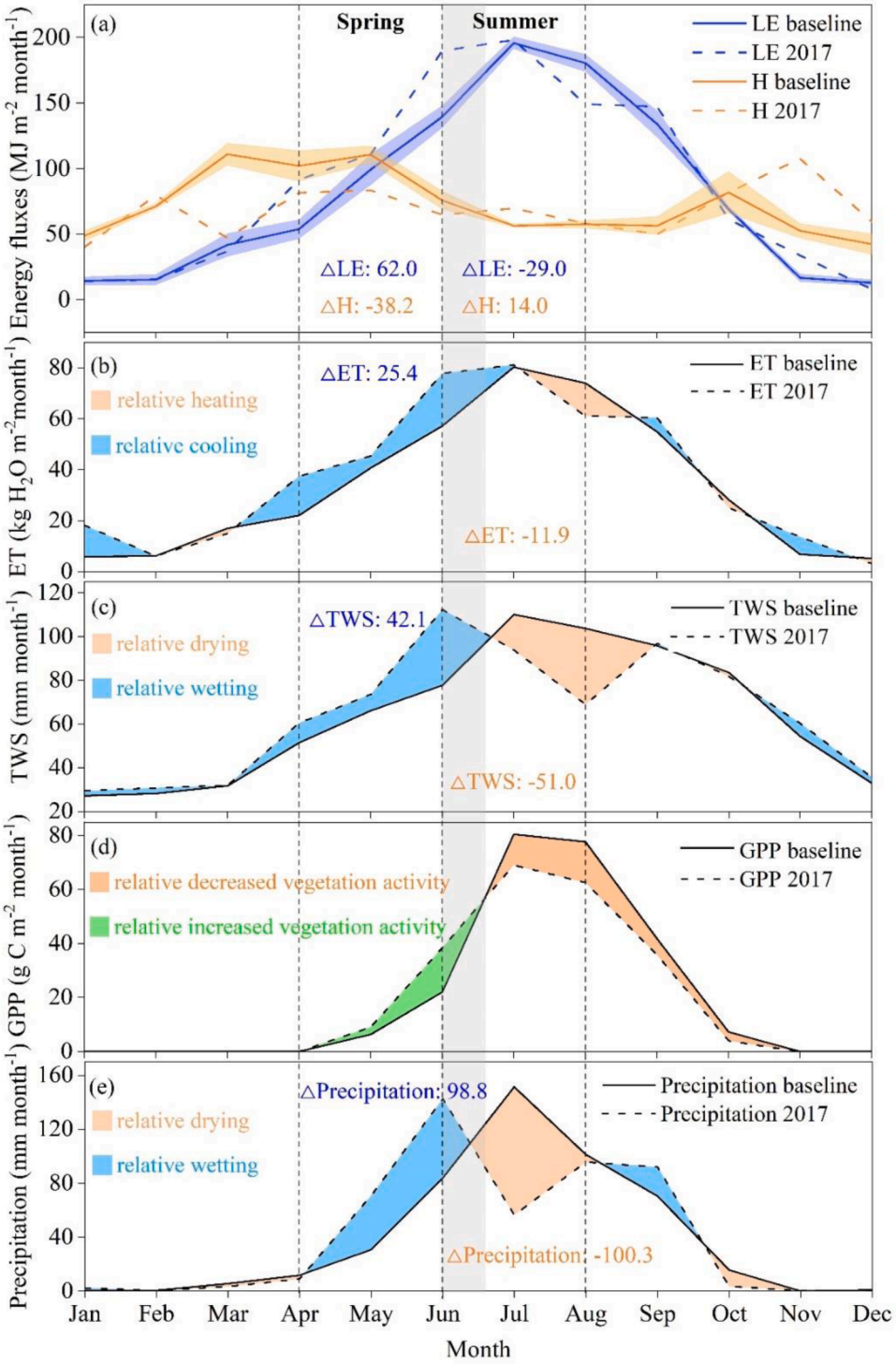

Fig. 4. The seasonal dynamic and anomalies of the water and heat fluxes under the landscape scale. (a). LE and H; (b). ET; (c).TWS; (d). GPP; (e). Precipitation. The numbers atop showed the mean seasonal anomalies. Shaded areas between the solid lines and the dotted lines represented the study variables' anomalies. The grey areas indicated the early summer drought.

Table 1
. The correlations of spring ET and summer TWS under the landscape scale based on PCOR and the Granger causality test for the above correlation.

	PCOR		Granger causality test	
	Coefficient	*p* -value	*F* values	*p* -value
Parameters	−0.53	**<0.001**	5.25	**0.03**

Control variables: DR, precipitation, and mean Ta.

3.4. The driving factors of the anomalies in GPP and ET under multiple scales observations

At the landscape scale, SEM results indicated that the positive anomalies of spring GPP and ET were primarily due to the indirect and beneficial effect ($p < 0.05$) of positive SWC anomalies on increasing LAI (Fig. 6a). In contrast, during the summer drought, the negative anomalies of GPP and ET were directly driven by the negative anomalies of

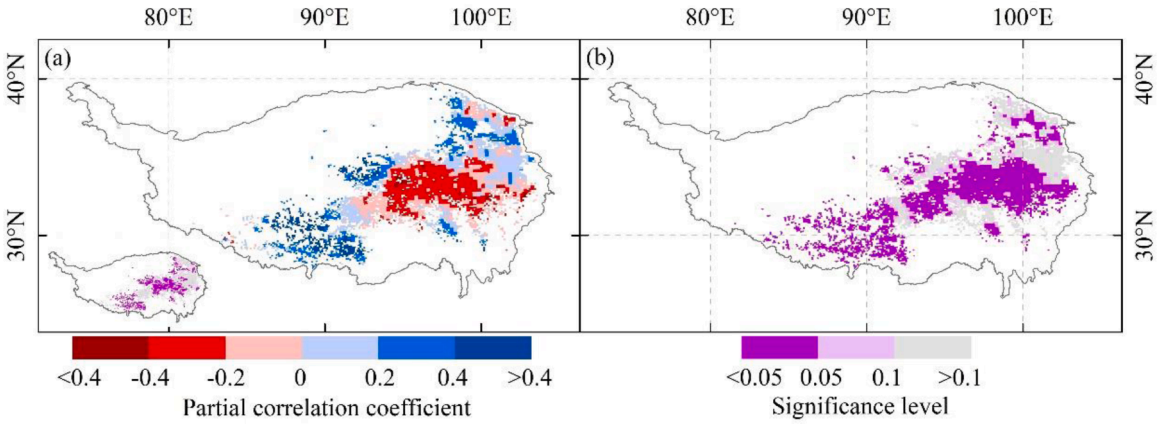

Fig. 5. The spatial distributions of the partial correlation coefficients of spring ET with summer SWC (a) and the Granger causality test for above correlations (b). The distributions of the significant correlations are shown in each panel's bottom-left corner ($p < 0.1$).

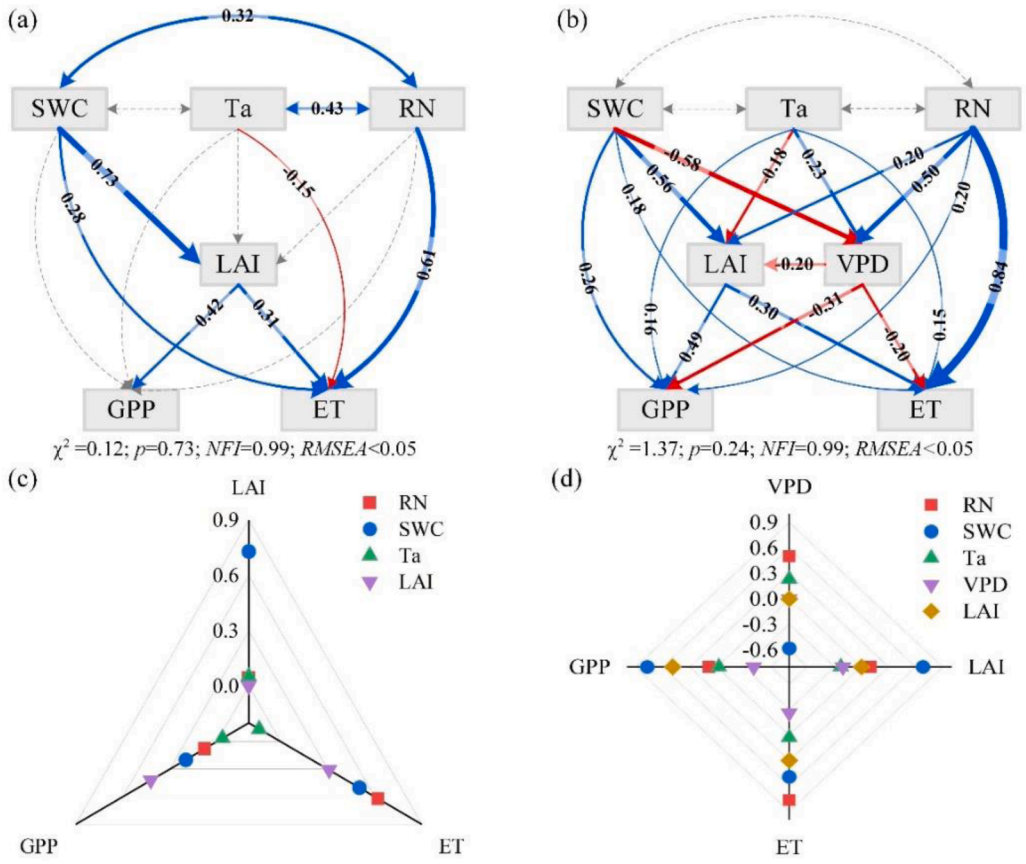

Fig. 6. SEM analysis reveals the impacts of abiotic and biotic factors on the anomalies of ET and GPP during (a) spring and (b) summer, and the standardized total effects of the variables during (c) spring and (d) summer. The solid (broken) arrows connecting the boxes indicate significant/insignificant paths at the p=0.05 level. The thickness of the lines shows the strength of the correlations, while the values adjacent to arrows are the standardized path coefficients. The blue/red arrows illustrate positive/negative relationships. Model statistics include the Root Mean Square Error of Approximation (RMSEA), Normed Fit Index (NFI), and Chi-square (χ^2). (For interpretation of the references to color in this figure, the reader is referred to the web version of this article.).

SWC (Fig. 6b; $p < 0.05$). SWC also indirectly influenced the negative anomalies of GPP and ET by decreasing LAI and increasing VPD (Fig. 6b; $p < 0.05$). Furthermore, positive VPD anomalies significantly ($p < 0.05$) and directly negatively influenced ET, GPP, and LAI anomalies during summer drought (Fig. 6b). The standardized total effects indicated that in comparison to mean Ta and VPD anomalies during spring and summer, SWC anomalies had a more significant impact on ET, LAI, and GPP anomalies (Fig. 6c,d). Furthermore, the indirect negative impacts of mean Ta anomalies on GPP anomalies through reducing LAI and increasing VPD were greater than its direct positive impacts during summer drought (Fig. 6b).

PCOR analysis revealed that the significant negative correlations ($p < 0.1$) of the anomalies in spring SWC and mean Ta with the green-up date anomalies occupied 20% and 15.4% of the study area, respectively (Fig. 7a,b,g). Then, in about 25% of the study area, the green-up dates anomalies significantly and negatively ($p < 0.1$) influenced spring NPP and ET anomalies based on PCOR (Fig. 7c,d). The significant correlations of the anomalies in summer SWC (positive) and VPD (negative) with summer NPP anomalies occupied 24.9% and 13.6% of the study area based on PCOR, respectively (Fig. 7e,f,h; $p < 0.1$). SWC anomalies had a higher impact on green-up dates and summer NPP anomalies than on spring mean Ta and summer VPD anomalies, consistent with the landscape scale (Fig. 7g,h).

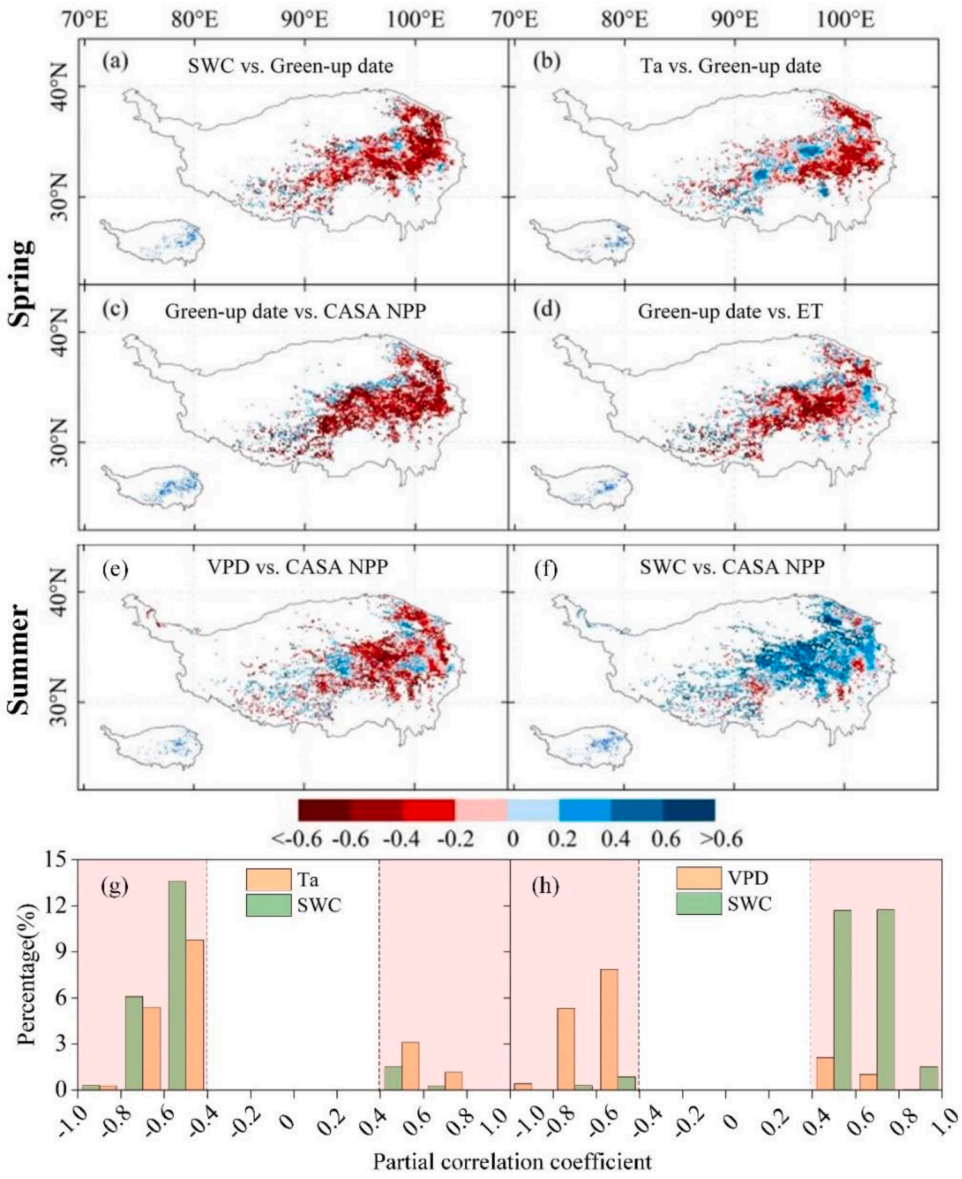

Fig. 7. The spatial distributions of the partial correlation coefficients of the anomalies in green-up dates, NPP, and ET with the anomalies in the environment variables. The distributions of the significant correlations are shown in the bottom-left corner of each panel ($p < 0.1$). Control variables: (a). mean Ta, DR, and precipitation; (b). SWC, DR, and precipitation; (c, d). mean Ta, SWC, DR, and precipitation; (e). mean Ta, DR, SWC, and precipitation; (f). mean Ta, DR, VPD, and precipitation; (g).The histogram of significant partial correlations of SWC (Ta) with green-up date; (h). VPD (SWC) with summer GPP.

3.5. The driving factors of lower Ta and its potential effects on GPP during summer drought

The negative mean Ta anomalies during the summer drought, fornotably for nighttime Ta, were revealed by multiple scales observations, prompting us to investigate their causes. Both MLR and RF analyses of the landscape-scale observations during the summer drought consistently indicated that nighttime DLR anomalies contributed more to nighttime Ta anomalies than nighttime TS, DR, H, and precipitation anomalies (Table 2; $p < 0.05$). Similarly, over 70% of the research area demonstrated that nighttime Ta anomalies were explained mainly by nighttime DLR anomalies compared to the anomalies in other variables on a regional scale (Fig. A.6; $p < 0.1$).

And then, we evaluated the potential impact of lower mean Ta resulting from lower nighttime Ta. When mean Ta was replaced by its baseline, the simulated VPD increased by 5.1% compared to the observed VPD during the summer drought (Fig. 8a). Based on the training model of the observed values in RF, $GPP_{Simliated}$ (predicted GPP

Table 2
The correlations of the anomalies of nighttime Ta with the anomalies of nighttime DLR, nighttime TS, H, DR, and precipitation based on MLR and RF under the landscape scale observations. Variance inflation factor: VIF

Variable	MLR				RF	
	coefficient	relweight	VIF	*p*-value	relweight	p-value
nighttime DLR	0.06	53.98	3.03	**<0.001**	70.66	**<0.01**
nighttime TS	0.37	15.09	1.55	**<0.001**	13.63	**<0.01**
H	−0.41	13.39	2.40	**<0.001**	6.54	>0.05
DR	0.11	12.01	4.15	**<0.001**	5.71	>0.05
precipitation	−0.04	5.53	1.72	>0.05	3.46	>0.05
R^2	0.78				0.74	

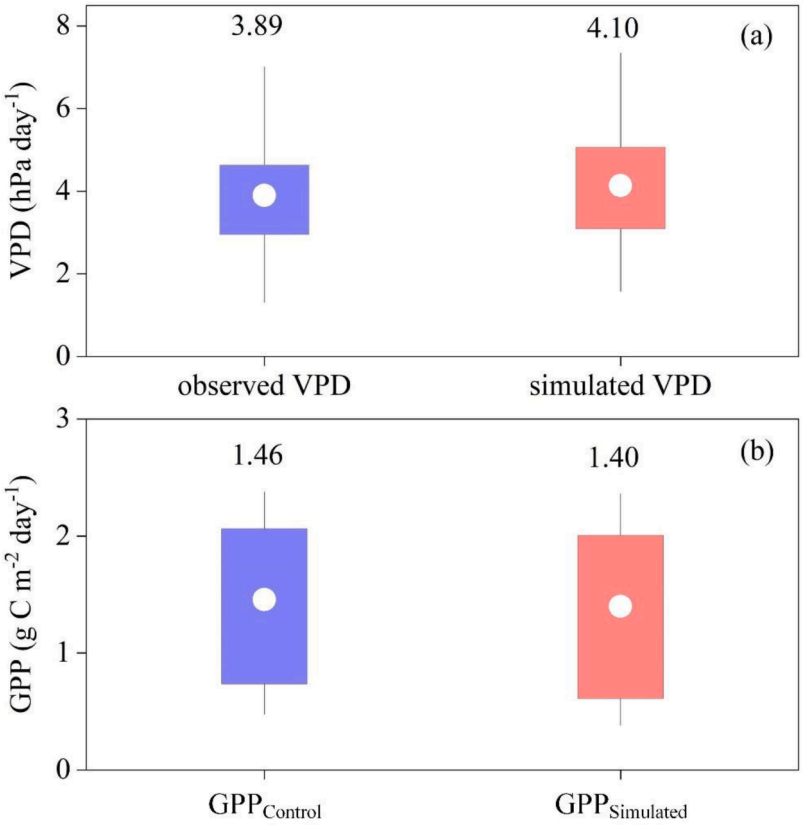

Fig. 8. Lower mean Ta and its potential impacts on GPP during summer drought. (a). The simulated VPD using baseline mean Ta and the observed VPD during summer drought; (b). $GPP_{Control}$ and $GPP_{Simulated}$. White dots and numbers atop indicated the mean values of the variables. Model: GPP~VPD+Ta+precipitation+PAR+SWC+LAI.

was estimated by the training models using simulated VPD and the baseline mean Ta) was 4.3% lower than $GPP_{Control}$ (predicted GPP was estimated by the training models using the observed values) during summer drought (Fig. 8b). This suggests that lower mean Ta can mitigate GPP declines through decreasing VPD during the summer drought.

4. Discussions

Spring carbon uptake would be boosted by earlier vegetative activity, compensating for its loss caused by summer drought (Fig. 9). However, higher ET induced by earlier vegetation activities could deplete soil water resources and thus exacerbate the summer water shortage mainly ascribed to decreasing precipitation (Fig. 9). The above-mentioned adverse effects on soil water availability would decrease the evaporative cooling by reducing summer LE (ET) shifting available energy partitioning toward H, thus contributing to positive heating feedback (Fig. 9). However, during the summer drought, our observations demonstrated decreased mean Ta due to reduced nighttime Ta caused by lower nighttime DLR (Fig. 9). Furthermore, lower mean Ta could mitigate carbon loss by declining VPD during the summer drought (Fig. 9). As a result, our findings highlight the importance of lower mean Ta and its buffering effects in understanding how the carbon and water cycles respond to the linked effects.

4.1. The positive effects of earlier vegetation activities on spring carbon uptake

Earlier vegetative activity, fueled mainly driven through adequate water availability, may increase spring carbon uptake. Field and remote sensing observations indicated that preseason and spring water supply had a substantial effect on the spring phenologytrend on the TP (Dorji et al., 2013; Shen et al., 2015a; Zhu et al., 2017). Similarly, findings from landscape scale demonstrated the negative associations between SWC and green-up dates, showing that enough SWC may contribute to earlier vegetative activities (Table A.1). This is primarily because *K. pygmaea*, as the dominant species in the alpine meadow, is a shallow-rooted plant that relies heavily on soil surface water, making it more susceptible to changes in water supply (Chen et al., 2019; Dorji et al., 2013). Although we recognized the significant impacts of spring mean Ta on the green-up dates (Zu et al., 2018), the effects of spring SWC anomalies on vegetation activities were stronger than Ta anomalies under the landscape and regional scales (Table A.1). Earlier greening would lengthen the period of active carbon absorption and improve spring carbon uptake, as recent studies have demonstrated (Fu et al., 2017; Ganjurjav et al., 2021; Zhu et al., 2017). Therefore, earlier vegetation activities could be beneficial to increased carbon uptake during spring and thus partly compensate for summer carbon loss induced by droughts.

4.2. The lagged effects of earlier vegetation activities on later water and heat fluxes

Recent research indicates that earlier vegetation activities may consume soil water resources earlier due to increased spring ET, hence exacerbating summer droughts (Wang et al., 2020; Wolf et al., 2016). Similarly, based on the long time series of remote sensing data, the ecosystem could be more vulnerable to summer water restrictions, partly due to the above-mentioned lagged impacts of earlier greening (Buermann et al., 2013; Buermann et al., 2018; Lian et al., 2020; Piao et al., 2019; Yu et al., 2018; Zeng et al., 2021). Our study aimed to demonstrate the phenomenon by presenting the following findings. First, despite considerable decreases in precipitation and TWS during the early stages of the summer drought, ET was greater than the

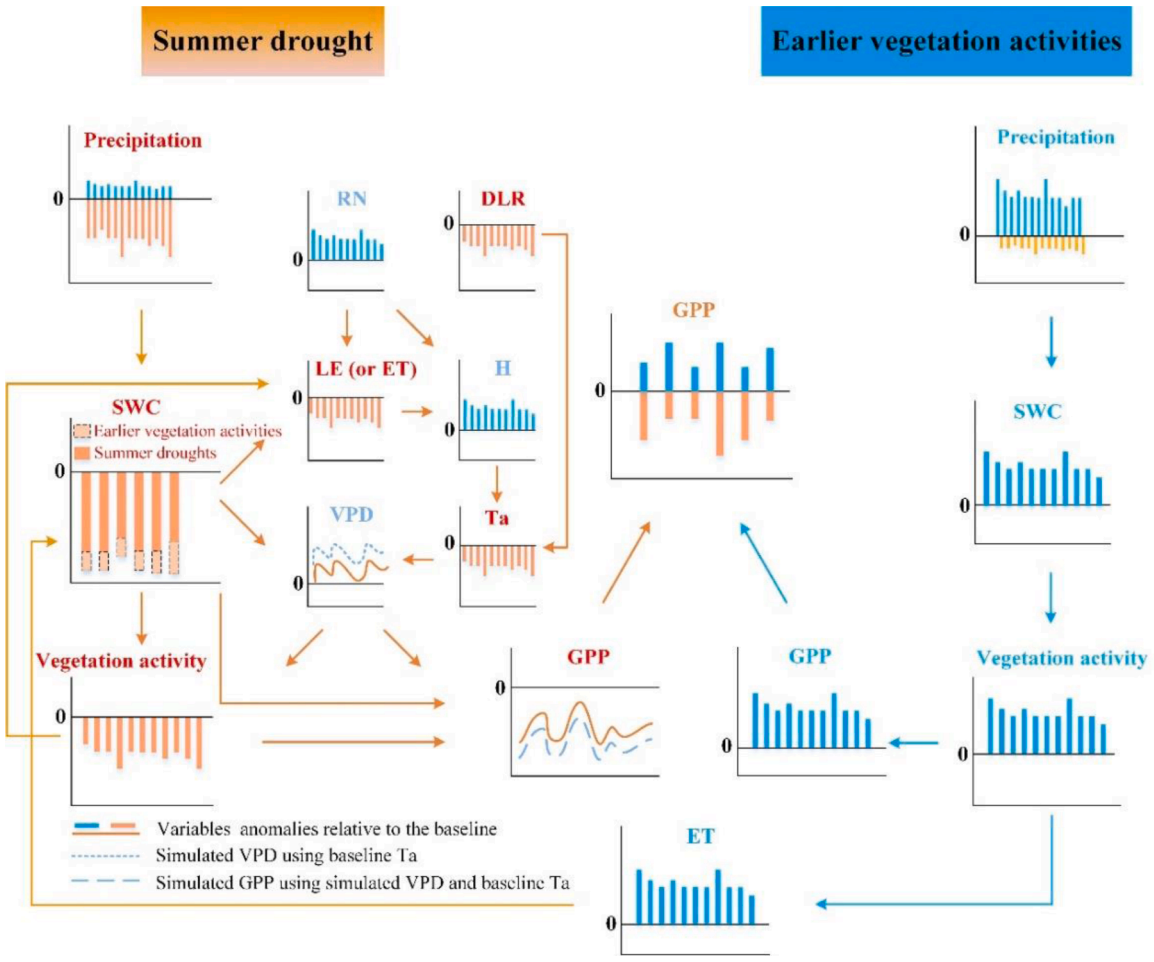

Fig. 9. Diagram illustrating the cascading effects of early vegetation activity and summer drought on the carbon and water fluxes.

baseline. To some extent, higher ET during this period may result in summer soil dryness because subsequent deficiency did not recover this water loss. Second, data at both landscape and regional scales consistently revealed a negative association between spring ET and summer soil water supplies, consistent with the Granger causality test. These findings suggest that increasing spring ET induced by earlier greening could exacerbate summer soil drying. Third, during the 2017 summer drought, our recent result showed that deep-layer SWC in grazed was higher than in fenced due to reduced ET is driven by grazing-induced reductions in LAI (Zhang et al., 2019a). This provided an additional explanation for the impact of ET on water consumption.

Water limitations caused by early vegetation activity and summer drought could weaken the evaporative cooling, changing the partitioning of available energy toward H, contributing to a positive heating feedback (Wolf et al., 2016). Additionally, our analysis discovered the similar anomalies in LE (ET) and H. During the summer drought, the mean Ta was lower than the baseline in multiple scales observations, particularly for nighttime Ta. Even though contradicts recent research indicating that positive heating feedback may contribute to a higher mean Ta during summer drought (Wang et al., 2020; Wolf et al., 2016), it is consistent with our recent observations (Chen et al., 2020b). One possible explanation for why the mean Ta was lower than baseline may be lower atmospheric counter radiation (lower DLR) induced by less cloud amount during drought. On the TP, high altitude, low air pressure, and thin air could significantly reduce the insulating properties of clouds, particularly during summer drought (Chen et al., 2020b). Our unpublished findings indicated that the TP experienced a more significant reduction in nighttime DLR and cloud amount than other regions during drought in China. The indirect effects of cloud cover on nighttime Ta through influencing nighttime DLR were stronger than other regions on the TP (Unpublished data). Moreover, frozen layer in permafrost zones is always composed of ice and soil, and hence the ice-water phase change would take a significant amount of energy (Zhao et al., 2004). Such consumption is more than 110 MJ m^{-2} in the permafrost regions of the TP, although the simulation values vary with the active layer thickness (Hu et al., 2015; Zhao et al., 2021). This suggests that heat propagating downward is further consumed by ice-water phase change, buffering the heating feedbacks as previously mentioned.

4.3. *The responses of summer GPP to soil and atmospheric water deficits*

Droughts can limit GPP and plant growth by aggravating soil water deficiencies (Chen et al., 2020a). The resistance of dominant species highly determines the affected degree of ecosystem functions caused by droughts (Helmut et al., 2008; Hoover et al., 2014). Due to its shallow roots and lower leaf relative water content, *K. pygmaea* is more susceptible to droughts (Dorji et al., 2013; Zhu et al., 2017). It is more sensitive to drying than to wetness (Chen et al., 2019). Due to *K. pygmaea's* lower resistance, its coverage is strongly restricted by soil water deficiencies (Chen et al., 2020b). Lower vegetation cover can minimize the canopy's photosynthetic capability and GPP (Chen et al., 2020a). According to SEM, droughts affect GPP due to the direct impact of lower SWC and the indirect effect of water scarcity-induced decreases in LAI.

As previously stated, lower mean Ta can compensate for drought-induced declines in GPP by decreasing VPD. Through the land-

atmosphere interactions, higher VPD is mostly determined by lower SWC and higher mean Ta during droughts (Chen et al., 2021; Kimm et al., 2020). Under high VPD conditions, plants tend to close their stomata to minimize water loss at the leaf scale, thus restricting photosynthetic activities (Monteith, 1995). Although VPD has a weaker impact on GPP than SWC during droughts on the TP (Chen et al., 2021; Zhang et al., 2018) and global scale (Liu et al., 2020), higher VPD also plays a vital role in restraining GPP and LAI during droughts (Chen et al., 2021; Kimm et al., 2020; Xu et al., 2021). Our multiple observations verified the above statements. According to RF's simulated results, lower mean Ta can offset-induced GPP declines by 4.3% by decreasing VPD by 5.1%. This shows that lower mean Ta could reduces VPD and then mitigate carbon loss during droughts.

4.4. Uncertainties and future research needs

There are a few aspects to consider in the future. First, the magnitudes of green-up dates and GPP varied among the site, landscape, and region scales observations. This bias may be explained by their measurement methods, spatial scales and datasets producting modes, etc (Chen et al., 2020a). Second, to our knowledge, present research cannot exactly quantify the actual water constraints and heating feedback induced by earlier vegetation activities. New experiments combining multiple factors (e.g., earlier spring × summer drought) are urgently needed to accurately measure above-mentioned hydrothermal feedbacks in future research. Third, although our findings of lower mean Ta during summer drought are guaranteed, the driving mechanisms and potential effects of lower mean Ta need deep analysis. Future research should examine energy partitioning in the TP's permafrost zones during the summer drought, including the ice-water phase. Model simulations should be used to assess the potential consequences of decreased mean Ta by taking into account the anomalies in LAI, VPD, and other variables.

5. Conclusion

The chained impacts of earlier vegetation activity and summer drought could substantially influence broad ecological processes. Currently, these effects on the TP remain elusive yet. We demonstrated that earlier spring partially compensated for summer carbon loss caused by drought and may exacerbate the summer water deficit. However, decreasing evaporative cooling caused by water deficit did not result in a rise in summer mean Ta. Decreasing mean Ta could buffer the passive impacts of drought on carbon uptake. Our findings emphasize the importance of knock-on effects of vegetation activity and summer drought in driving the carbon and water cycles on the TP. Notably, more research is needed to fully comprehend the underlying mechanisms and potential consequences of decreased mean Ta during the summer drought. They may be favorable to accurately anticipate the response of ecological processes to summer drought in the future.

Data availability statement

Correspondence and requests for materials should be addressed to Yangjian Zhang.

Declaration of Competing Interest

The authors declare that they have no conflicts of interest.

Acknowledgments

This work was supported by the outstanding youth scientist program of NSFC (Grant No. 41725003), the National Natural Science Foundation of China (Grant No. 41991234; 42101109; 42071133), the National Key Research & Development Program (Grant No. 2019YFA0607302), and the China Postdoctoral Science Foundation-funded project (Grant No. 2020M681058). The authors gratefully acknowledge the contribution of CMFD and GLASS ET study datasets from the National Tibetan Plateau/Third Pole Environment Data Center (http://data.tpdc.ac.cn/zh-hans/) and National Earth System Science Data Center (http://www.geodata.cn/data/publisher.html), respectively.

Supplementary materials

Supplementary material associated with this article can be found, in the online version, at doi:10.1016/j.agrformet.2022.108975.

References

Bothe, O., Fraedrich, K., Zhu, X., 2011. Large-scale circulations and Tibetan Plateau summer drought and wetness in a high-resolution climate model. Int. J. Climatol. 31 (6), 832–846.
Buermann, W., Bikash, P.R., Jung, M., Burn, D.H., Reichstein, M., 2013. Earlier springs decrease peak summer productivity in North American boreal forests. Environ. Res. Lett. 8 (2), 024027.
Buermann, W., et al., 2018. Widespread seasonal compensation effects of spring warming on northern plant productivity. Nature 562 (7725), 110.
Cai, W., Xu, X., Sun, J., 2012. An investigation into the surface energy balance on the southeast edge of the Tibetan Plateau and the cloud's impact. AcMeS 70, 837–846.
Chen, H., et al., 2013. The impacts of climate change and human activities on biogeochemical cycles on the Qinghai-Tibetan Plateau. Glob. Chang. Biol. 19 (10), 2940–2955.
Chen, N., et al., 2021. Divergent impacts of atmospheric water demand on gross primary productivity in three typical ecosystems in China. Agric. For. Meteorol. 307, 108527.
Chen, N., et al., 2020a. Multiple-scale negative impacts of warming on ecosystem carbon use efficiency across the Tibetan Plateau grasslands. Global Ecol. Biogeogr. 30 (2), 398–413.
Chen, N., et al., 2019. Temperature-mediated responses of carbon fluxes to precipitation variabilities in an alpine meadow ecosystem on the Tibetan Plateau. Ecol. Evol. 9 (16), 9005–9017.
Chen, N., et al., 2020b. The compensation effects of post-drought regrowth on earlier drought loss across the tibetan plateau grasslands. Agric. For. Meteorol. 281, 107822.
Ding, J., et al., 2018. Increasingly important role of atmospheric aridity on Tibetan alpine grasslands. Geophys. Res. Lett. 45 (6), 2852–2859.
Dorji, T., et al., 2013. Plant functional traits mediate reproductive phenology and success in response to experimental warming and snow addition in Tibet. Glob. Chang. Biol. 19 (2), 459–472.
Fischer, M.L., et al., 2012. Carbon, water, and heat flux responses to experimental burning and drought in a tallgrass prairie. Agric. For. Meteorol. 166-167 (1), 169–174.
Frank, D., et al., 2015. Effects of climate extremes on the terrestrial carbon cycle: concepts, processes and potential future impacts. Glob. Chang. Biol. 21 (8), 2861–2880.
Fu, Z., et al., 2017. Climate controls over the net carbon uptake period and amplitude of net ecosystem production in temperate and boreal ecosystems. Agric. For. Meteorol. 243.
Ganjurjav, H., et al., 2021. Phenological changes offset the warming effects on biomass production in an alpine meadow on the Qinghai–Tibetan Plateau. J. Ecol. 109 (2), 1014–1025.
He, J., et al., 2020a. The first high-resolution meteorological forcing dataset for land process studies over China. Sci. Data 7 (1), 1–11.
He, J., et al., 2020b. The first high-resolution meteorological forcing dataset for land process studies over China. Sci. Data 7 (1), 25.
Helmut, H., Bennett, D.M., Cadotte, M.W., 2008. Consequences of dominance: a review of evenness effects on local and regional ecosystem processes. Ecology 89 (6), 1510–1520.
Hoover, D.L., Knapp, A.K., Smith, M.D., 2014. Resistance and resilience of a grassland ecosystem to climate extremes. Ecology 95 (9), 2646–2656.
Hu, G., et al., 2015. Modeling permafrost properties in the Qinghai-Xizang (Tibet) Plateau. Sci. China Earth Sci. 58 (12), 2309–2326.
Huang, K., et al., 2021. The confounding effect of snow cover on assessing spring phenology from space: a new look at trends on the Tibetan Plateau. Sci. Total Environ. 756, 144011.
Janssens, I.A., et al., 2003. Europe's terrestrial biosphere absorbs 7 to 12% of European anthropogenic CO_2 emissions. Science 300 (5625), 1538–1542.
Kimm, H., et al., 2020. Redefining droughts for the U.S. Corn belt: the dominant role of atmospheric vapor pressure deficit over soil moisture in regulating stomatal behavior of Maize and Soybean. Agric. For. Meteorol. 287, 107930.
Li, H., et al., 2016. Seasonal and inter-annual variations in CO 2 fluxes over 10 years in an alpine shrubland on the Qinghai-Tibetan Plateau, China. Agric. For. Meteorol. 228-229, 95–103.
Li, L., Yang, S., Wang, Z., Zhu, X., Tang, H., 2018. Evidence of warming and wetting climate over the Qinghai-Tibet Plateau. Arct. Antarct. Alp. Res. 42 (4), 449–457.
Li, M., et al., 2021. Declining human activity intensity on alpine grasslands of the Tibetan Plateau. J. Environ. Manag. 296, 113198.

Li, X., Xiao, J., 2019. Mapping photosynthesis solely from solar-induced chlorophyll fluorescence: a global, fine-resolution dataset of gross primary production derived from OCO-2. Remote Sens. 11 (21), 2563.
Lian, X., et al., 2020. Summer soil drying exacerbated by earlier spring greening of northern vegetation. Sci. Adv. 6 (1), eaax0255.
Liu, L., et al., 2020. Soil moisture dominates dryness stress on ecosystem production globally. Nat. Commun. 11 (1), 4892.
Martens, B., et al., 2017. GLEAM v3: satellite-based land evaporation and root-zone soil moisture. Geosci. Model Dev. 10 (5), 1903–1925.
Monteith, J.L., 1995. A reinterpretation of stomatal responses to humidity. Plant Cell Environ. 18 (4), 357–364.
Parazoo, N.C., et al., 2018. Spring photosynthetic onset and net CO2 uptake in Alaska triggered by landscape thawing. Glob. Chang. Biol. 24 (8), 3416–3435.
Piao, S., et al., 2019. Plant phenology and global climate change: current progresses and challenges. Glob. Chang. Biol. 25 (6), 1922–1940.
Potter, C.S., et al., 1993. Terrestrial ecosystem production: a process model based on global satellite and surface data. GBioC 7 (4), 811–841.
Shen, M., Piao, S., Cong, N., Zhang, G., Jassens, I.A., 2015a. Precipitation impacts on vegetation spring phenology on the Tibetan Plateau. Glob. Chang. Biol. 21 (10), 3647–3656.
Shen, M., et al., 2015b. Evaporative cooling over the Tibetan Plateau induced by vegetation growth. Proc. Natl. Acad. Sci. U. S. A., 112 (30), 9299–9304.
Shen, M., Tang, Y., Chen, J., Zhu, X., Zheng, Y., 2011. Influences of temperature and precipitation before the growing season on spring phenology in grasslands of the central and eastern Qinghai-Tibetan Plateau. Agric. For. Meteorol. 151 (12), 1711–1722.
Wallace, J.M., Hobbs, P.V., 2006. Atmospheric Science: An Introductory Survey, 92. Elsevier.
Wang, S., et al., 2020. Warmer spring alleviated the impacts of 2018 European summer heatwave and drought on vegetation photosynthesis. Agric. For. Meteorol. 295, 108195.
Wang, X., et al., 2019. No trends in spring and autumn phenology during the global warming hiatus. Nat. Commun. 10 (1), 2389.
Wolf, S., et al., 2016. Warm spring reduced carbon cycle impact of the 2012 US summer drought. Proc. Natl. Acad. Sci. U. S. A. 113 (21), 5880–5885.
Xu, M., et al., 2021. Drought limits alpine meadow productivity in northern Tibet. Agric. For. Meteorol. 303, 108371.
Yao, Y., et al., 2015a. A satellite-based hybrid algorithm to determine the Priestley–Taylor parameter for global terrestrial latent heat flux estimation across multiple biomes. Remote Sens. Environ. 165, 216–233.
Yao, Y., Zhang, Y., Zhao, S., Li, X., Jia, K., 2015b. Evaluation of three satellite-based latent heat flux algorithms over forest ecosystems using eddy covariance data. Environ. Monit. Assess. 187 (6), 382.
Yin, D., Roderick, M.L., Leech, G., Sun, F., Huang, Y., 2014. The contribution of reduction in evaporative cooling to higher surface air temperatures during drought. Geophys. Res. Lett. 41 (22), 7891–7897.
Yu, Z., et al., 2018. Earlier leaf-flushing suppressed ecosystem productivity by draining soil water in the Mongolian Plateau. Agric. For. Meteorol. 250, 1–8.
Zeng, Z., et al., 2021. Legacy effects of spring phenology on vegetation growth under preseason meteorological drought in the Northern Hemisphere. Agric. For. Meteorol. 310.
Zhang, G., Zhang, Y., Dong, J., Xiao, X., 2013. Green-up dates in the Tibetan Plateau have continuously advanced from 1982 to 2011. Proc. Natl. Acad. Sci. U. S. A. 110 (11), 4309–4314.
Zhang, T., et al., 2019a. Grazing-induced increases in soil moisture maintain higher productivity during droughts in alpine meadows on the Tibetan Plateau. Agric. For. Meteorol. 269-270, 249–256.
Zhang, T., et al., 2018. Water availability is more important than temperature in driving the carbon fluxes of an alpine meadow on the Tibetan Plateau. Agric. For. Meteorol. 256-257, 22–31.
Zhang, X., et al., 2003. Monitoring vegetation phenology using MODIS. Remote Sens. Environ. 84 (3), 471–475.
Zhang, Y., Zhu, Y., Li, J., Chen, Y., 2019b. Current status and future directions of the Tibetan Plateau ecosystem research. Sci. Bull. 64 (7), 428–430.
Zhao, L., et al., 2021. Dynamics and characteristics of soil temperature and moisture of active layer in the central Tibetan Plateau. Geoderma 400, 115083.
Zhao, L., et al., 2004. Changes of climate and seasonally frozen ground over the past 30 years in Qinghai–Xizang (Tibetan) Plateau, China. GPC 43 (1-2), 19–31.
Zhu, J., Zhang, Y., Jiang, L., 2017. Experimental warming drives a seasonal shift of ecosystem carbon exchange in Tibetan alpine meadow. Agric. For. Meteorol. 233, 242–249.
Zu, J., et al., 2018. Biological and climate factors co-regulated spatial-temporal dynamics of vegetation autumn phenology on the Tibetan Plateau. IJAEO 69, 198–205.